PHOTONICS Research

Electrically injected GeSn lasers with peak wavelength up to 2.7 μm

YIYIN ZHOU,[1,2] SOLOMON OJO,[1,2] CHEN-WEI WU,[3] YUANHAO MIAO,[1] HUONG TRAN,[1]
JOSHUA M. GRANT,[1,2] GREY ABERNATHY,[1,2] SYLVESTER AMOAH,[1] JAKE BASS,[1] GREGORY SALAMO,[4,5]
WEI DU,[6] GUO-EN CHANG,[3] JIFENG LIU,[7] JOE MARGETIS,[8] JOHN TOLLE,[8] YONG-HANG ZHANG,[8]
GREG SUN,[9] RICHARD A. SOREF,[9] BAOHUA LI,[10] AND SHUI-QING YU[1,5,*]

[1]*Department of Electrical Engineering, University of Arkansas, Fayetteville, Arkansas 72701, USA*
[2]*Microelectronics-Photonics Program, University of Arkansas, Fayetteville, Arkansas 72701, USA*
[3]*Department of Mechanical Engineering, Taiwan Chung-Cheng University, Ming-Hsiung, Chiayi 62102, China*
[4]*Department of Physics, University of Arkansas, Fayetteville, Arkansas 72701, USA*
[5]*Institute for Nanoscience and Engineering, University of Arkansas, Fayetteville, Arkansas 72701, USA*
[6]*Department of Electrical Engineering and Physics, Wilkes University, Wilkes-Barre, Pennsylvania 18766, USA*
[7]*Thayer School of Engineering, Dartmouth College, Hanover, New Hampshire 03755, USA*
[8]*School of Electrical, Energy and Computer Engineering, Arizona State University, Tempe, Arizona 85287, USA*
[9]*Department of Electrical Engineering, University of Massachusetts Boston, Boston, Massachusetts 02125, USA*
[10]*Arktonics, LLC, Fayetteville, Arkansas 72701, USA*
*Corresponding author: syu@uark.edu

GeSn lasers enable the monolithic integration of lasers on the Si platform using all-group-IV direct-bandgap material. The GeSn laser study recently moved from optical pumping into electrical injection. In this work, we present explorative investigations of GeSn heterostructure laser diodes with various layer thicknesses and material compositions. Cap layer material was studied by using $Si_{0.03}Ge_{0.89}Sn_{0.08}$ and $Ge_{0.95}Sn_{0.05}$, and cap layer total thickness was also compared. The 190 nm SiGeSn-cap device had threshold of 0.6 kA/cm² at 10 K and a maximum operating temperature (T_{max}) of 100 K, compared to 1.4 kA/cm² and 50 K from 150 nm SiGeSn-cap device, respectively. Furthermore, the 220 nm GeSn-cap device had 10 K threshold at 2.4 kA/cm² and T_{max} at 90 K, i.e., higher threshold and lower maximal operation temperature compared to the SiGeSn cap layer, indicating that enhanced electron confinement using SiGeSn can reduce the threshold considerably. The study of the active region material showed that device gain region using $Ge_{0.87}Sn_{0.13}$ had a higher threshold and lower T_{max}, compared to $Ge_{0.89}Sn_{0.11}$. The performance was affected by the metal absorption, free carrier absorption, and possibly defect density level. The maximum peak wavelength was measured as 2682 nm at 90 K by using $Ge_{0.87}Sn_{0.13}$ in gain regions. The investigations provide directions to the future GeSn laser diode designs toward the full integration of group-IV photonics on a Si platform. © 2021 Chinese Laser Press

https://doi.org/10.1364/PRJ.443144

1. INTRODUCTION

SiGeSn alloys have attracted considerable attention in recent years as a versatile material system enabling all-group-IV-based optoelectronic device integration [1,2]. Specifically, direct-bandgap GeSn offers a route toward monolithic integration of light sources on Si for mid-infrared applications [3]. The first set of GeSn lasers was demonstrated under optical pumping at temperatures up to 90 K [4]. Since then, the studies of GeSn lasers have made inspiring leaps in maximum operating temperature (T_{max}) up to near room temperature [5–7], with expanded wavelength coverage up to 4.6 μm [8], and with reduced thresholds of continuous-wave operation [9]. The

comparison between ridge waveguide lasers and micro-disk lasers provided further insight into the importance of optical confinement and heat dissipation [10]. Studies of the optically pumped lasers ranged from bulk lasers [11] to heterostructures [6] and multiple-quantum-well lasers [12,13]. The threshold was reduced by introducing carrier-confinement structures. Furthermore, an increase in the Sn composition of the GeSn active region led to lasing at elevated temperatures [6,7]. All these effects were studied under optical pumping.

The electrically injected GeSn laser diode is of even greater interest, as it can be fully integrated on the Si-based group-IV photonics platform. However, to achieve lasing under electrical

injection involves more challenges than that under optical pumping. For example, extra sources of optical loss are introduced by the metal contacts and doping. The metal is highly absorptive so that extra layers are needed to isolate the metal away from the optical mode while maintaining a decent electrical conduction. Such layers require more precise control during the material growth. Another challenge is the increased free carrier absorption (FCA) loss due to increased doping for more effective carrier injection through a pn junction, which increases laser threshold in comparison with optically pumped lasers, where carrier injection is easily achieved with the optical absorption of the pump light.

Such differences illustrate the need to design and evaluate the laser structures under electrical injection. Recently, an electrically pumped laser operational up to 100 K was demonstrated [14]. The devices had a minimum threshold at 0.6 kA/cm^2 and maximum peak power output of 2.7 mW per facet at 10 K. Compared to using n-type contact on the top surface, placing p-type contact on the top limited the hole leakage from the type II band alignment between the cap layer and the active region. The thick active region and the low refractive index cap layer offered an optical confinement factor of 75%. Although this specific design leads to demonstration of electrically pumped lasers, still uncharted are the effects of layer thicknesses and alloy gain medium/barrier material selections, which offers fundamental guidance for future GeSn diode laser design.

In this work, several electrically injected GeSn heterostructure laser diodes with different cap layers and active layer materials were compared. Increased cap thickness improves the optical confinement factor in the gain region and reduces the optical loss from the metal contact significantly. The devices with a thicker cap layer demonstrated reduced threshold, compared to the devices with a thinner cap. Cap layer materials with different conduction band barrier heights were also studied. The $Si_{0.03}Ge_{0.89}Sn_{0.08}$ capped devices with a 114 meV barrier height exhibited a lower threshold and higher T_{max}, compared to the devices with $Ge_{0.95}Sn_{0.05}$ cap with a 58 meV barrier height, which is due to the improvement on the electron confinement. Devices with 11% and 13% Sn composition in the GeSn active region are compared to probe the effect of intrinsic GeSn gain within the laser diode. Beyond the observation that lasing at a longer wavelength was recorded at 2682 nm at 90 K,

the increase of Sn composition did not show improvement on threshold and T_{max}, implying that extrinsic structure property deteriorates the performance.

2. EXPERIMENT

A. Layer Structure of the Laser Diodes

The sample structures were grown on the 200 mm Si (100) wafer using reduced pressure chemical vapor deposition. The five layers were epitaxially grown in the sequence of (i) a 500 nm Ge buffer, n-type doped (phosphorus) at 1×10^{19} cm^{-3}; (ii) a 700 nm spontaneous-relaxation-enhanced GeSn buffer, n-type doped at 1×10^{19} cm^{-3}; (iii) a 1000 nm GeSn active region, undoped; (iv) the first GeSn or SiGeSn cap layer with p-type doping (boron) at 1×10^{18} cm^{-3}; (v) a 50 nm (Si)GeSn cap layer with p-type doping at 1×10^{19} cm^{-3}. The GeSn buffer layers had a varied Sn composition: 7%–11% in samples A to D and 10%–13% in sample E. The GeSn active region had a composition of 11% in samples A to D and 13% in sample E. The dislocations induced by the crystalline strain relaxation are expected within the GeSn buffer layer. The relaxation leads to a Sn gradient within the GeSn buffer. The dislocations are expected to cause a Sn gradient within the GeSn buffer and confined within some few hundreds of nanometers. The GeSn active region was then grown with the same recipe and low defect density. The standard *in situ* dopant gas was introduced to form the n-type and p-type regions. A schematic of the laser structure is described in Fig. 1(a). The device actual thickness, composition, and the corresponding conduction band barrier height ΔE_c between the cap layer and active region are summarized in Table 1.

B. Device Fabrication

The laser diode devices were fabricated into ridge waveguide laser structure. The 80 μm wide ridge structure was formed by standard photolithography and wet chemical etching. The ridge was etched to the n-type GeSn buffer (200 nm etched into the buffer layer). The metal contacts (10 nm Cr + 350 nm Au) were deposited by using an electron beam evaporator. The Si substrate on the back side was reduced to ~140 μm thickness by lapping, followed by a cleaving to form the facets. The cavity length falls between 1.2 and 1.7 mm. The laser diodes were wire-bonded onto a Si carrier with isolated Au bonding pads.
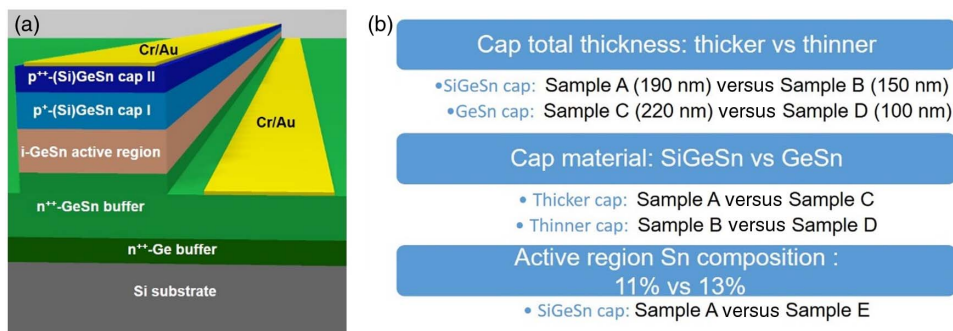

Fig. 1. (a) 3D schematic of the ridge waveguide laser designed structure; (b) three experiment groups are studied with tuning of the total cap thickness, cap layer material, and active region Sn composition.

Table 1.   Summary of Laser Structure

Sample	p-type Cap			GeSn Active Region		n-type Buffer	
	Material	Thickness (nm)	ΔE_c^* (meV)	Sn Composition (%)	Thickness (nm)	Material	Thickness (nm)
A	$Si_{0.03}Ge_{0.89}Sn_{0.08}$	190	114	11.2	610	$Ge_{0.93}Sn_{0.07}$	950
B	$Si_{0.03}Ge_{0.89}Sn_{0.08}$	150	114	10.8	430	$Ge_{0.93}Sn_{0.07}$	670
C	$Ge_{0.95}Sn_{0.05}$	220	58	11.2	520	$Ge_{0.93}Sn_{0.07}$	650
D	$Ge_{0.95}Sn_{0.05}$	100	58	11.5	450	$Ge_{0.93}Sn_{0.07}$	610
E	$Si_{0.03}Ge_{0.89}Sn_{0.08}$	180	131	13.1	540	$Ge_{0.93}Sn_{0.07}$	540

C. Experimental Design

Three sets of experiments were designed to study the GeSn laser structures, summarized in Fig. 1(b). The first set adjusts the total thickness of the cap layer in order to evaluate the optical mode-profile effect on the optical confinement factor as well as the absorption loss. Samples A and C have the designed total cap thickness of 190 nm compared to 150 nm in samples B and D, respectively. The second variable is the material used in the cap layers that changes conduction-band barrier height in the heterostructure. $Si_{0.03}Ge_{0.89}Sn_{0.08}$ with 114 meV of barrier height is used in samples A and B, compared to $Ge_{0.95}Sn_{0.05}$ with 58 meV barrier height used in samples C and D. The last experiment evaluates the device performance affected by the Sn composition in the GeSn active region. Sample E has a nominal 13% of Sn in the active region, compared to 11% in sample A. Note that sample A, which was reported in Ref. [14], served as a reference in this work.

D. Experimental Methods

The photoluminescence (PL) was measured from the cap-removed sample. The heterostructure sample was chemically etched, the top 600 nm of the structure was removed, and the active region was exposed at the surface for PL characterization. The sample surface was excited by using the 532 nm continuous-wave laser at 500 mW. The emission was collected through the spectrometer with the InSb detector. The signal was recorded via a standard lock-in technique.

For the electrically injected laser measurement, the chip was mounted in a temperature-controlled cryostat for the characterization. The device operated under a pulsed mode to avoid Joule heating. The pulsed voltage source was used as the pumping source with a 1 kHz repetition rate and 700 ns of pulse width. The emission power and spectra were characterized using a grating-based spectrometer equipped with a liquid-nitrogen-cooled InSb detector (detection range 1.0–5.5 μm). The spectra presented in this paper focus on comparing the peak wavelength and on demonstrating the emission below and above the lasing threshold. Therefore, the resolution of the spectrometer is set at 10 nm, which is compromised to obtain a reasonable signal-to-noise ratio for the spectrum, especially at the low intensity level below the threshold. The absolute optical power was measured using a calibrated power meter. The emission from the facet was coupled by a pair of convex lenses and focused on the power meter. Note that the reflection and absorption losses through the cryostat window and lens were calculated and were added to the power meter readout aiming to report more accurate emission power. The emission was then guided onto the InSb detector through the spectrometer for the light output-current injection (L-I) and spectral measurements.

The detailed description of the high-resolution spectra and the absolute power calibration process can be found in Ref. [14].

3. RESULTS

A. Observation of Lasing

To validate the lasing operation, the devices characteristics were measured using the same method that was detailed in Ref. [14]. According to measurement results, all devices show unambiguous lasing characteristics, as the threshold indicating the onset of lasing, dramatically reduced peak linewidth, and increased peak intensity were clearly observed, which were acknowledged to identify the lasing of sample A in Ref. [14]. The typical characterization results of sample E are shown in Fig. 2.

Figure 2(a) displays the temperature-dependent L-I curves for sample E. The threshold characteristic can be clearly resolved. The lasing was observed at temperatures from 10 K to 90 K, with the threshold from 1.4 to 3.6 kA/cm². The characteristic temperature T_0 was extracted as 81 K. The maximum power output was measured of 0.7 mW/facet under 4 kA/cm² at 30 K. From 10 K to 50 K, the kink can be observed at $\sim 1.5 \times J_{th}$, which may be due to the switch of the lasing mode.

Figure 2(b) shows the emission spectra below and above the lasing threshold at 10 K. The PL spectrum at 10 K was also plotted for comparison (dotted line). Compared to the PL peak, the significantly reduced emission peak linewidth indicates the onset of lasing. Note that based on our previous study [5,7,14], the devices feature multimode operation, and therefore the observed peak actually consists of multimode peaks [e.g., see the spectra in Fig. 2(b) for $1.2 \times J_{th}$ and that in Fig. 2(c) for $1.0 \times J_{th}$], which cannot be further resolved due to the spectrometer resolution of 10 nm. As current injection increases to above threshold, a narrower linewidth peak sitting on background spontaneous emission emerges, whose intensity dramatically increases at $1.2 \times J_{th}$. This trend indicates the unambiguous lasing characteristic. The lasing peak wavelength was measured as 2654 nm at $1.2 \times J_{th}$ and 10 K. The emission spectra at 90 K are plotted in Fig. 2(c). The spontaneous emission (at $0.9 \times J_{th}$) from the active region cannot be resolved due to the low intensity. In a semi-log plot, below threshold ($0.9 \times J_{th}$), a broad peak at ~ 2600 to 3000 nm with relatively weak intensity was obtained, suggesting the spontaneous emission. The linewidth difference between stimulated and spontaneous emission can be clearly identified from the semi-log spectra. The intensity of the broad emission peak has barely changed intensity as the injection increased, which is due to the pinning of the carrier
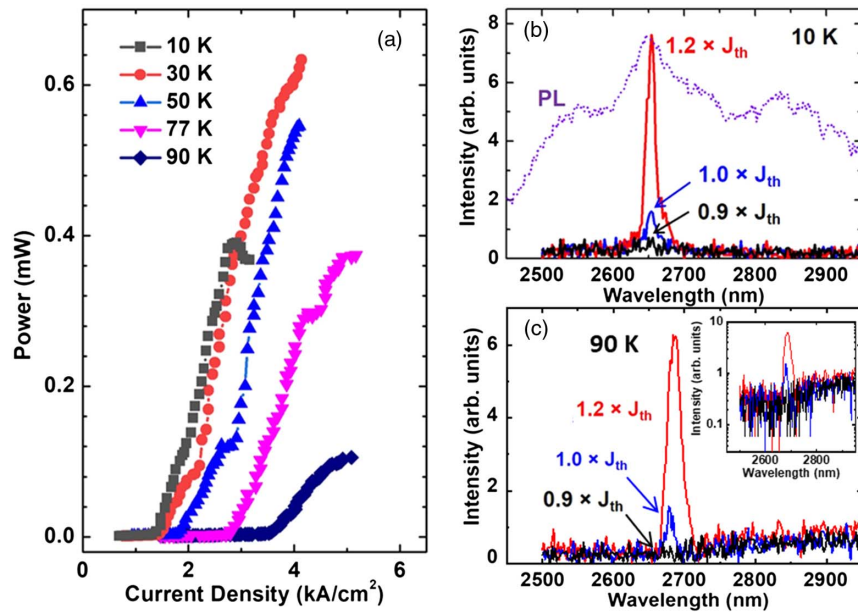
Fig. 2. Characterizations of sample E. (a) Temperature-dependent L-I curve. (b) Lasing spectra under injections below and above threshold at 10 K. The PL spectrum was also plotted for comparison. (c) Emission spectra under injections below and above threshold at 90 K; inset: semi-log plot of the spectra.

density contributing to the spontaneous emission. The lasing peak can be clearly identified at injection above the threshold. Under injection of $1.2 \times J_{th}$ at 90 K, the lasing wavelength was measured as 2682 nm.

B. Light Output-Current Injection Characteristics

The L-I curves of all devices at 10 K are plotted in Fig. 3(a). Sample A features the lowest threshold while sample D has the highest threshold, which are 0.6 and 3.4 kA/cm^2, respectively. It is worth noting that regarding the curve slope above the threshold, samples A, C, and E exhibit similar slope, which is higher than that of samples B and D. Sample A reached the maximum power output of 2.25 mW/facet under 3.5 kA/cm^2, which is the highest among all five samples. Sample C has the second highest maximum output power at 1.05 mW/facet under 5.5 kA/cm^2.

As temperature increases, sample D stops lasing above 10 K. Figure 3(b) shows L-I curves of all other samples at 50 K. The lowest and highest thresholds are 0.8 kA/cm^2 (sample A) and 2.5 kA/cm^2 (sample C), respectively. Sample B shows a lower curve slope above the threshold compared to the other three samples.

As temperature further increases, sample B stops lasing above 50 K. The L-I curves of samples A, C, and E at 90 K are shown in Fig. 3(c), with the corresponding thresholds of 1.8, 5.1, and 3.6 kA/cm^2, respectively. The maximum operational temperature of samples C and E is 90 K, while for sample A it is 100 K, which has been reported in Ref. [14].

Figure 4 shows the laser peak emission under injection of $1.1 \times J_{th}$ as a function of temperature. At 10 K, the lasing peak of sample A was obtained at 2240 nm. For samples B, C, and D
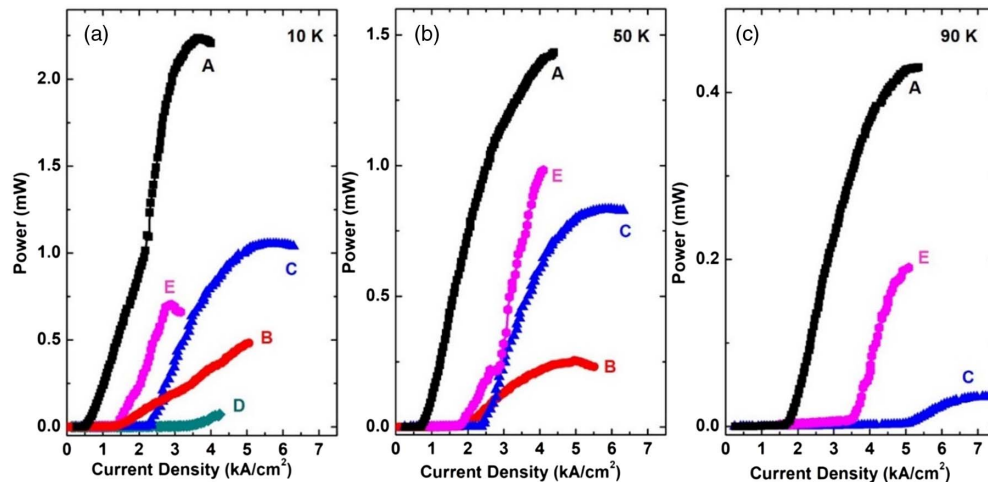

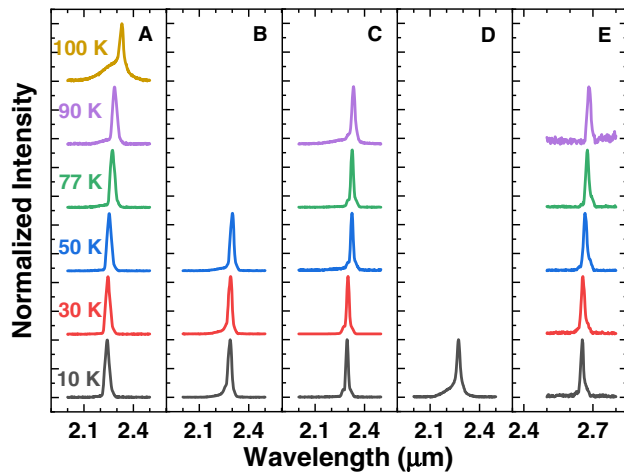**Fig. 3.** L-I curves of each sample at (a) 10 K, (b) 50 K, and (c) 90 K.

Fig. 4. Normalized spectra showing the lasing peaks under $1.1 \times J_{th}$ injection for each sample at the corresponding operational temperatures.

the lasing peaks were observed at ~2270–2290 nm. This is due to the slight difference of Sn compositions in the active region. The lasing peak of sample E is at 2654 nm, much longer than the rest of the samples due to the higher Sn composition (13% versus 11%) in the active region. As the temperature increases, the peak emission shifts toward longer wavelength as expected, which represents a narrower bandgap at higher temperature. At 90 K, the lasing peak was obtained at 2682 nm for sample E. Note that the lasing spectral peak shift is almost equivalent to the temperature shift of bandgap energy, i.e., following the Varshni relation: $E_{GeSn}(T) = E_{GeSn}(0) - \alpha T^2/(T + \beta)$, where $E_{GeSn}(0)$ is the bandgap energy at 0 K, and α and β are the material-dependent parameters. The values of α and β were studied in our previous work [15], which are comparable to a III-V material system ($\alpha \sim 10^{-4}$ eV/K^2 and $\beta \sim 200$ K).

For samples A to E, the full widths at half-maximum (FWHMs) incorporating all lasing modes were measured as 32, 29, 18, 34, and 16 nm (under the 10 nm resolution spectrometer), respectively, at 10 K. Note that these FWHMs represent the gain spectral width rather than the true lasing peak width since each incorporates a series of longitudinal modes that cannot be resolved at 10 nm resolution. Our previous studies revealed that due to the relatively large area of the cross section, all laser devices feature multimode operation. The high-resolution lasing spectra showing well-resolved multipeaks of sample A were reported in Ref. [14]. The characteristics for all laser devices are summarized in Table 2.

4. DISCUSSION

A. Thickness of Cap Layer [First Experimental Group in Fig. 1(b)]

The total thickness of the cap layer considerably affects the lasing performance. Both comparisons (A versus B and C versus D) show the same trend, no matter whether SiGeSn or GeSn is used as cap layer material—that a thicker cap device has a lower lasing threshold as well as higher maximum operating temperature: at 10 K, sample A has a threshold that is 0.43 of that of sample B, while sample C has a lower threshold that is 0.70 of sample D. For the maximum operating temperature, 100 K for sample A versus 50 K for sample B, and 90 K for sample C versus 10 K for sample D, were observed. The change of cap layer thickness affects the laser performance by the following factors: (i) optical loss from the metal contact playing the major role, (ii) FCA within the heavily doped cap layers, and (iii) the optical confinement factor in the active region.

The optical loss on the metal contacts was originated from the imaginary part of the refractive index [16]. The metal absorption was extracted from the dielectric waveguide simulation. Using the structure in sample A, the metal absorption loss is plotted as a function of SiGeSn cap total thickness in Fig. 5. The metal absorption loss is reduced from 1287 to 554 cm^{-1} (from sample B to A) and from 1724 to 720 cm^{-1} (from sample D to C) when the cap thickness increases from ~100 (B and D) to ~200 nm (A, C, and E). As the cap layer thickness increases from 100 to 1200 nm, the absorption loss decreases to as low as 1 cm^{-1}. The calculated metal absorption loss for each sample is summarized in Table 3. Compared to other sources of optical loss, the metal absorption is the dominating loss mechanism in the structure. Note that the metal scattering loss is not counted here.

The FCA loss for each layer was calculated based on the doping level and the carrier injection [17] as summarized in Table 3. A considerable amount of FCA is introduced in the active region, serving as the second dominating loss mechanism. The n-type-doped GeSn buffer shows a relatively small value (6–11 cm^{-1}) in each sample, while the p-type-doped cap layer exhibits higher values (36 and 72 cm^{-1}). In the active region, the FCA level is taken, assuming high injection at 5.0×10^{18} cm^{-3}. Sample E exhibits a higher FCA loss due to a longer emission wavelength. In Fig. 5, the FCA in the p-type cap was plotted as a function of cap thickness using the structure of sample A. The FCA in the cap increases as the cap thickness increases. The combination of metal absorption and FCA in the cap can be reduced to ~110 cm^{-1} as the

Table 2. Summary of Laser Characteristics[a]

Sample	Cap Layer Material	Cap Layer Thickness (nm)	Sn Composition in Active Region (%)	Threshold at 10 K (kA/cm^2)	Threshold at 77 K (kA/cm^2)	T_{max} (K)	T_0^a (K)	Lasing Wavelength at 10 K (nm)
A	$Si_{0.03}Ge_{0.89}Sn_{0.08}$	190	11	0.6	1.4	100	76	2238
B	$Si_{0.03}Ge_{0.89}Sn_{0.08}$	150	11	1.4	N.A.	50	119	2281
C	$Ge_{0.95}Sn_{0.05}$	220	11	2.4	3.1	90	123	2294
D	$Ge_{0.95}Sn_{0.05}$	100	11	3.4	N.A.	10	N.A.	2272
E	$Si_{0.03}Ge_{0.89}Sn_{0.08}$	180	13	1.4	2.9	90	81	2654

[a]T_0 is extracted from 10 K to the maximum lasing temperature (T_{max}).
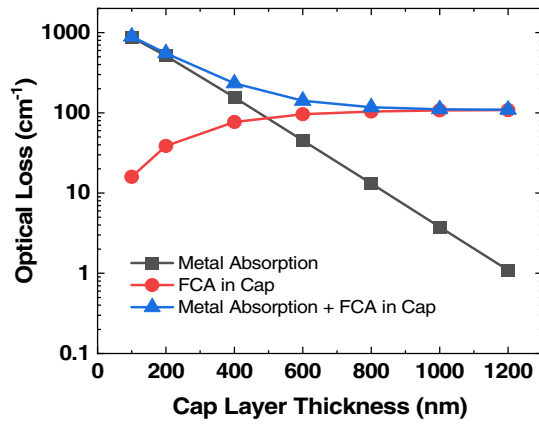
Fig. 5. Calculated metal absorption loss and FCA loss in p-type cap layer for sample A as functions of SiGeSn cap layer total thickness.

cap thickness reaches beyond 800 nm. This promises that the total loss for sample A can be reduced by half at the threshold.

Overall, it can be seen that the higher total loss results in a larger threshold, comparing B to A (or D to C). The metal absorption loss dramatically decreases as the cap layer thickness increases, while the FCA loss shows limited change. As a result, the total loss would not further decrease with the thicker cap. Moreover, with very thick cap layer (~1000 nm), the optical confinement in the active region may decrease due to the relatively small refractive index difference (~0.2) between the active region and cap. On the other hand, since the critical thickness of the SiGeSn cap on GeSn is less than 100 nm, the further relaxation of SiGeSn would result in material degradation due to the generation of dislocations.

B. Cap Layer Materials [Second Experimental Group in Fig. 1(b)]
The cap layer also serves as the top energy barrier with respect to active region. The $Si_{0.03}Ge_{0.89}Sn_{0.08}$ and $Ge_{0.95}Sn_{0.05}$ are compared as the cap layer materials. Note that both cap materials feature tensile strain due to relatively smaller lattice constants with respect to the active layer, leading to type II band alignment being obtained in the light hole (LH) in the valence band (VB) at the cap/active interface, which creates a hole leakage channel. This issue was addressed by injecting holes from the top so that the holes flow from the p-type cap layer toward the n-type GeSn buffer, where the barrier at the active/GeSn buffer interface could confine the holes in the active region as described in Ref. [14]. Therefore, the electron confinement offered by cap layers is a focus in this experiment.

The conduction band (CB) barrier height of each sample was calculated. For both comparisons (A versus C and B versus D: $Si_{0.03}Ge_{0.89}Sn_{0.08}$ versus $Ge_{0.95}Sn_{0.05}$), regardless of the cap layer thickness, the samples using $Si_{0.03}Ge_{0.89}Sn_{0.08}$ cap have the barrier height of 114 meV, while the samples using $Ge_{0.95}Sn_{0.05}$ cap show a lower barrier height of 58 meV. The higher barrier height improves the device performance due to better electron confinement. (i) At 10 K, sample A has a much lower threshold that is 0.25 of that of sample C, while sample B has a threshold that is 0.41 of sample D. The similar threshold reduction was also reported on III-V laser devices [18]. (ii) For the maximum operating temperature, 100 K for sample A versus 90 K for sample C, and 50 K for sample B versus 10 K for sample D, were obtained. As temperature increases, due to increased thermal energy k_BT that can be absorbed by carriers, the electron confinement capability is weakened, leading to the result that the samples using $Ge_{0.95}Sn_{0.05}$ cap (lower barrier height) stop lasing prior to those using $Si_{0.03}Ge_{0.89}Sn_{0.08}$ cap (higher barrier height). Note that, for sample D, because of its thin $Ge_{0.95}Sn_{0.05}$ cap (100 nm), it can only lase at 10 K.

The VB barrier height between the GeSn active and the GeSn buffer was calculated for each sample as well. Samples A to D show similar hole barrier height of ~30 meV. At room temperature, such a barrier is merely more than one k_BT, and therefore it is insufficient for hole confinement. A wider bandgap material, i.e., SiGeSn, can be used to replace the GeSn buffer for higher band barrier height in VB, to enhance hole confinement.

Note that the accurate band offset has not been experimentally verified so far, and the actual band alignment remains uncertain. However, the difference between barrier height has its significance to show the general laser structure behavior qualitatively.

C. Sn Compositions in the Active Region [Third Experimental Group in Fig. 1(b)]
Samples A ($Ge_{0.89}Sn_{0.11}$) and E ($Ge_{0.87}Sn_{0.13}$) are compared for the active region materials. Our previous studies on GeSn optically pumped lasers indicated that the increase of Sn composition in the active region led to the increase of the maximum operating temperature and reduction of lasing threshold [5–7]. This is attributed to the higher-Sn-induced greater directness of bandgap in the active region, which facilitates the electron populating the Γ valley. However, in this experiment, the electrically injected device with higher Sn composition neither shows reduced threshold nor exhibits increased operating temperature: at 10 and 77 K, the thresholds of sample E (1.4 and

Table 3. Calculated Loss and Threshold at 10 K

Sample	Metal Absorption Loss (cm^{-1})	P-type Cap FCA Loss (cm^{-1})	Active Region FCA Loss (cm^{-1})	N-type Buffer FCA Loss (cm^{-1})	Mirror Loss (cm^{-1})	Total Loss (cm^{-1})	Threshold at 10 K (kA/cm^2)
A	554	39	383	6	6	988	0.6
B	1287	51	320	7	8	1673	1.4
C	720	72	443	9	8	1252	2.4
D	1724	36	341	11	8	2120	3.4
E	1557	70	753	11	8	2399	1.4

2.9 kA/cm^2) are doubled compared to those of sample A (0.6 and 1.4 kA/cm^2); the maximum lasing temperature of 90 K for sample E is 10 K lower than that of sample A. This can be interpreted as follows. (i) The total loss is calculated higher in sample E than in sample A. This is mainly due to the thinner well of sample E that leads to larger modal overlap with metal layer and elevated FCA loss at longer emission wavelength. (ii) The optically pumped lasers rely on optical absorption to collect the carriers. For a certain wavelength of incident light, the absorption coefficient increases as Sn composition in the GeSn active region increases due to narrower bandgap. However, for electrically injected lasers, the carrier injection efficiency does not show obvious improvement with sample E. Characterization of band offset could provide more detailed information. (iii) The GeSn active region with higher Sn composition has a larger lattice constant. The increased lattice mismatch between the active region and the buffer leads to increased dislocation density in the active region. Such dislocations serve as the nonradiative recombination center that reduces the carrier injection efficiency. Recent studies on GeSn double heterostructure LEDs show similar issue that an increase of Sn composition does not directly improve the emission intensity [19,20]. Therefore, a higher Sn composition in GeSn buffer might be helpful to maintain the high-quality active region. (iv) Sample A has a slightly larger cavity length of 1.7 mm compared to 1.3 mm for sample E. The longer cavity features reduced mirror loss, leading to a better performance. Note that the difference of mirror loss between samples A and E is relatively small (6 cm^{-1} versus 8 cm^{-1}) compared to other loss, and thus it is not a dominant factor in this experiment.

D. Additional Consideration

In addition to the abovementioned loss mechanism, other factors that affect the device performance are elaborated as follows. (i) Active layer thickness. In this work, the design of sample structure is inherited from the former optically pumped lasers, in which a thicker active layer is preferred, aiming to have higher light absorption. However, such absorption enhancement with a thicker active layer does not apply to electrically injected lasers. In fact, growing a thinner active region could effectively reduce the threshold [21]. (ii) Absorption loss in the GeSn buffer and the SiGeSn/GeSn cap. Since the GeSn buffer is almost relaxed and heavily doped, the high density of dislocations due to lattice mismatch would create defect energy levels in the bandgap, resulting in additional absorption loss. The absorption tails have been reported in GeSn materials, which leads to below-bandgap absorption with the orders of 1–10 cm^{-1} for extra loss [22,23]. Likewise, once the thicker cap layer beyond the critical thickness is employed, the gradually relaxed material would introduce a considerable density of dislocations. Therefore, the lattice-matched cap layer is desirable, which again relies on the advance of SiGeSn material growth capability. (iii) The scattering loss induced by sidewall roughness. The relatively rough sidewall would result in additional scattering loss, especially for the device with a relatively narrow ridge. Reducing the sidewall roughness by improving the fabrication procedure is a viable solution to reduce the scattering loss.

5. CONCLUSIONS

In conclusion, electrically injected GeSn laser diodes were studied with an evaluation of three factors in the structure: cap layer thickness, cap materials, and active region materials. The thicker capped devices feature lower metal absorption loss, offering a reduction of threshold and an elevation of maximum operating temperature. The devices with a $Si_{0.03}Ge_{0.89}Sn_{0.08}$ cap show lower threshold and higher maximum operating temperature compared to the devices using a $Ge_{0.95}Sn_{0.05}$ cap, which is due to the higher barrier height at the active/cap interface when employing the $Si_{0.03}Ge_{0.89}Sn_{0.08}$ cap. The 13% Sn in the active region, however, does not improve the device performance in terms of lasing threshold and temperature compared to an 11% Sn device, when the same $Si_{0.03}Ge_{0.89}Sn_{0.08}$ cap was used. The performance of high-Sn composition devices can be improved by employing a thinner active layer and a cap with less lattice mismatch, which could reduce the dislocation density. The maximum lasing peak wavelength was measured as 2682 nm at 90 K from the devices with $Ge_{0.87}Sn_{0.13}$ in the active region.

Disclosures.   The authors declare no conflicts of interest.

Data Availability.   Data underlying the results presented in this paper are not publicly available at this time but may be obtained from the authors upon reasonable request.

REFERENCES

1. R. Soref, "Mid-infrared photonics in silicon and germanium," Nat. Photonics **4**, 495–497 (2010).
2. R. Soref, D. Buca, and S.-Q. Yu, "Group IV photonics: driving integrated optoelectronics," Opt. Photon. News **27**, 32–39 (2016).
3. X. Wang and J. Liu, "Emerging technologies in Si active photonics," J. Semicond. **39**, 061001 (2018).
4. S. Wirths, R. Geiger, N. von den Driesch, G. Mussler, T. Stoca, S. Mantl, Z. Ikonic, M. Luysberg, S. Chiussi, J. M. Hartmann, H. Sigg, J. Faist, D. Buca, and D. Grützmacher, "Lasing in direct-bandgap GeSn alloy grown on Si," Nat. Photonics **9**, 88–92 (2015).
5. J. Margetis, S. Al-Kabi, W. Du, W. Dou, Y. Zhou, T. Pham, P. Grant, S. Ghetmiri, A. Mosleh, B. Li, J. Liu, G. Sun, R. Soref, J. Tolle, M. Mortazavi, and S.-Q. Yu, "Si-based GeSn lasers with wavelength coverage of 2–3 μm and operating temperatures up to 180 K," ACS Photon. **5**, 827–833 (2017).
6. Q. Thai, N. Pauc, J. Aubin, M. Bertrand, J. Chrétien, V. Delaye, A. Chelnokov, J. Hartmann, V. Reboud, and V. Calvo, "GeSn heterostructure micro-disk laser operating at 230 K," Opt. Express **26**, 32500–32508 (2018).
7. Y. Zhou, W. Dou, W. Du, S. Ojo, H. Tran, S. Ghetmiri, J. Liu, G. Sun, R. Soref, J. Margetis, J. Tolle, B. Li, Z. Chen, M. Mortazavi, and S.-Q. Yu, "Optically pumped GeSn lasers operating at 270 K with broad waveguide structures on Si," ACS Photon. **6**, 1434–1441 (2019).
8. J. Chrétien, N. Pauc, F. Armand Pilon, M. Bertrand, Q. Thai, L. Casiez, N. Bernier, H. Dansas, P. Gergaud, E. Delamadeleine, R. Khazaka, H. Sigg, J. Faist, A. Chelnokov, V. Reboud, J. Hartmann, and V. Calvo,

"GeSn lasers covering a wide wavelength range thanks to uniaxial tensile strain," ACS Photon. **6**, 2462–2469 (2019).

9. A. Elbaz, D. Buca, N. von den Driesch, K. Pantzas, G. Patriarche, N. Zerounian, E. Herth, X. Checoury, S. Sauvage, I. Sagnes, A. Foti, R. Ossikovski, J. Hartmann, F. Boeuf, Z. Ikonic, P. Boucaud, D. Grützmacher, and M. El Kurdi, "Ultra-low threshold cw and pulsed lasing in tensile strained GeSn alloys," Nat. Photonics **14**, 375–382 (2020).

10. W. Du, Q. M. Thai, J. Chrétien, M. Bertrand, L. Casiez, Y. Zhou, J. Margetis, N. Pauc, A. Chelnokov, V. Reboud, V. Calvo, J. Tolle, B. Li, and S.-Q. Yu, "Study of Si-based GeSn optically pumped lasers with micro-disk and ridge waveguide structures," Front. Phys. **7**, 147 (2019).

11. D. Stange, S. Wirths, R. Geiger, C. Schulte-Braucks, B. Marzban, N. von den Driesch, G. Mussler, T. Zabel, T. Stoica, J.-M. Hartmann, S. Mantl, Z. Ikonic, D. Grützmacher, H. Sigg, J. Witzens, and D. Buca, "Optically pumped GeSn microdisk lasers on Si," ACS Photon. **3**, 1279–1285 (2016).

12. D. Stange, N. von den Driesch, T. Zabel, F. Armand-Pilon, D. Rainko, B. Marzban, P. Zaumseil, J. Hartmann, Z. Ikonic, G. Capellini, S. Mantl, H. Sigg, J. Witzens, D. Grützmacher, and D. Buca, "GeSn/SiGeSn heterostructure and multi quantum well lasers," ACS Photon. **5**, 4628–4636 (2018).

13. J. Margetis, Y. Zhou, and W. Dou *et al.* et al., "All group-IV SiGeSn/GeSn/SiGeSn QW laser on Si operating up to 90 K," Appl. Phys. Lett. **113**, 221104 (2018).

14. Y. Zhou, Y. Miao, S. Ojo, H. Tran, G. Abernathy, J. M. Grant, S. Amoah, G. Salamo, W. Du, J. Liu, J. Margetis, J. Tolle, Y.-H. Zhang, G. Sun, R. A. Soref, B. Li, and S.-Q. Yu, "Electrically injected GeSn lasers on Si operating up to 100 K," Optica **7**, 924–929 (2020).

15. S. A. Ghetmiri, W. Du, B. R. Conley, A. Mosleh, A. Nazzal, G. Sun, R. A. Soref, J. Margetis, T. Joe, H. A. Naseem, and S. Q. Yu, "Shortwave-infrared photoluminescence from Ge$_{1-x}$Sn$_x$ thin films on silicon," J. Vac. Sci. Technol. B **32**, 060601 (2014).

16. E. Garmire and H. Stoll, "Propagation losses in metal-film-substrate optical waveguides," IEEE J. Quantum Electron. **8**, 763–766 (1972).

17. G. E. Chang, S. W. Chang, and S. L. Chuang, "Theory for n-type doped, tensile-strained Ge-Si$_x$Ge$_y$Sn$_{1-x-y}$ quantum-well lasers at telecom wavelength," Opt. Express **17**, 11246–11258 (2009).

18. C. Chaminant, J. Charil, J.-C. Bouley, and E. V. K. Rao, "Growth and properties of GaAsSb/GaAlAsSb double heterostructure lasers," IEEE Trans. Electron. Dev. **3**, 196–200 (1979).

19. Y. Zhou, W. Dou, W. Du, T. Pham, S. A. Ghetmiri, S. Al-Kabi, A. Mosleh, M. Alher, J. Margetis, J. Tolle, G. Sun, R. Soref, B. Li, M. Mortazavi, H. Naseem, and S.-Q. Yu, "Systematic study of GeSn heterostructure-based light-emitting diodes towards mid-infrared applications," J. Appl. Phys. **120**, 023102 (2016).

20. M. Bertrand, N. Pauc, Q. M. Thai, J. Chrétien, L. Casiez, A. Quintero, P. Rodriguez, R. Khazaka, J. Aubin, J. M. Hartmann, A. Chelnokov, V. Calvo, and V. Reboud, "Mid-infrared GeSn-based LEDs with Sn content up to 16%," in *IEEE 16th International Conference on Group IV Photonics* (2019), pp. 1–2.

21. S. L. Chuang, Physics of Photonic Devices, 2nd ed. (Wiley Publishing), Chapter 10, pp. 416–417.

22. S. V. Kondratenko, Yu. V. Hyrka, Yu. I. Mazur, A. V. Kuchuk, W. Dou, H. Tran, J. Margetis, J. Tolle, S.-Q. Yu, and G. J. Salamo, "Photovoltage spectroscopy of direct and indirect bandgaps of strained Ge$_{1-x}$Sn$_x$ thin films on a Ge/Si(001) substrate," Acta Mater. **171**, 40–47 (2019).

23. H. Tran, W. Du, S. Ghetmiri, A. Mosleh, G. Sun, R. Soref, J. Margetis, J. Tolle, B. Li, H. Naseem, and S.-Q. Yu, "Systematic study of Ge$_{1-x}$Sn$_x$ absorption coefficient and refractive index for the device applications of Si-based optoelectronics," J. Appl. Phys. **119**, 103106 (2016).